PERGAMON

International Journal of Solids and Structures 38 (2001) 1433–1458

INTERNATIONAL JOURNAL OF SOLIDS and STRUCTURES

www.elsevier.com/locate/ijsolstr

Modeling diffusional coarsening in eutectic tin/lead solders: a quantitative approach

W. Dreyer [a,1], W.H. Müller [b,*]

[a] *Weierstraß Institut für Angewandte Analysis und Stochastik, Mohrenstraße 39, 10117 Berlin, Germany*
[b] *Department of Mechanical and Chemical Engineering, Heriot-Watt University, Riccarton, Edinburgh EH14 4AS, UK*

Received 10 December 1999; in revised form 12 March 2000

Abstract

This paper presents a quantitative simulation of the phase separation and coarsening phenomenon in eutectic tin/lead (SnPb) solders. The computer modeling is based on continuum theory and phase field models that were evaluated using the most recently available data for the free energy of the tin/lead system, diffusional and mobility coefficients, elastic constants as well as surface tensions of both phases. The model presented allows us to study the influence as well as the interaction between classical diffusion of the Fickean type, surface energies according to Cahn and Hilliard, as well as stresses and strains on phase separation and coarsening. An attempt is made to compare the temporal development of a eutectic SnPb microstructure at different temperature levels and subjected to different stress levels as predicted by the model to actual experiments.

Keywords: Modeling; Coarsening; Tin/lead solders

1. Introduction

1.1. The technical dimension

Reliable joining techniques are crucial during manufacture and reliable operation of micro-electronic packages. In particular, most recently there has been a considerable interest in the reliability and lifetime of solder joints, which are used extensively in Surface Mount Technology (SMT) (see, e.g., Lau, 1995). Examples of SMT components include Ball Grid Arrays (BGAs), Chip Scale Packages (CSPs), or Flip Chips (FCs), as shown in Fig. 1. All of these use tin/lead solder (SnPb) to electrically and mechanically connect a silicon wafer to a Printed Circuit Board (PCB). Clearly, thermal mismatch between the various materials involved in microelectronic structures is inevitable although serious attempts are made to keep it as small as possible. This mismatch in combination with advanced temperatures is the key issue in solder joint

* Corresponding author. Tel.: +44-131-451-3689; fax: +44-131-451-3129.
E-mail address: w.h.muller@hw.ac.uk (W.H. Müller).
[1] All names are in alphabetical order. Both authors contributed equally to this article.

0020-7683/01/$ - see front matter
PII: S0020-7683(00)00103-7

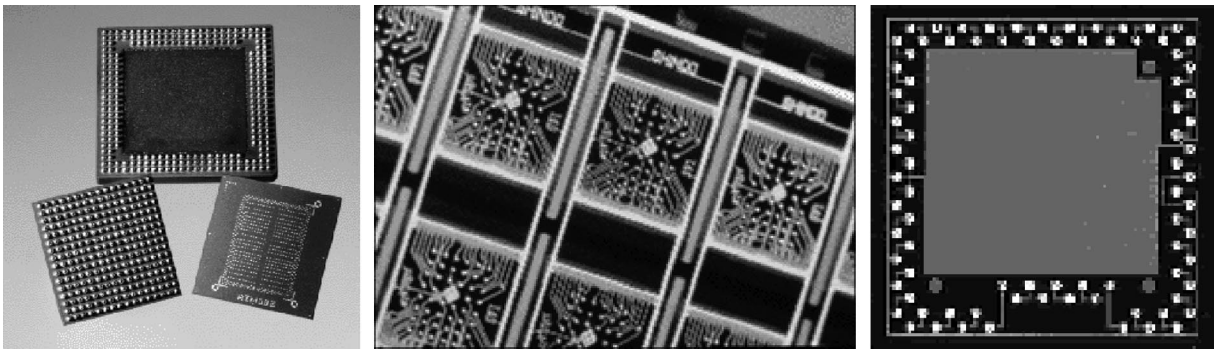

Fig. 1. A few examples of SMT components (from left to right): BGAs, CSPs, and an FC before mount (Hauck et al., 2000).

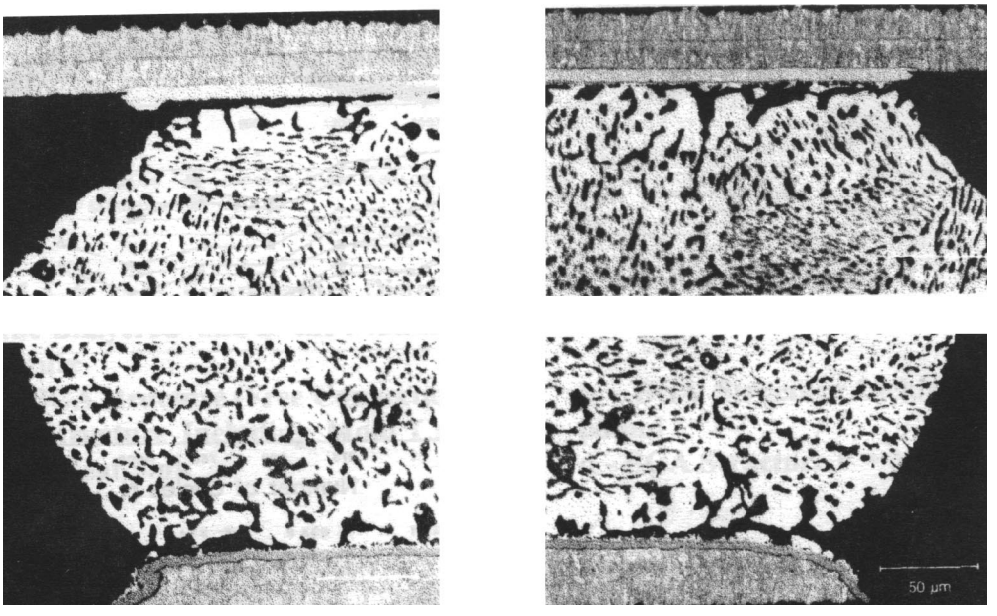

Fig. 2. Cross-sectional cut through a BGA solder bump made of PbSn after several thousand power cycles (Albrecht and Gamalski, 1996); severe signs of coarsening by phase separation are visible together with interface crack formation at intermetallic phase boundaries.

reliability. As an example, consider Fig. 2 which presents a cross-sectional cut through a BGA solder bump, after it has been subjected to several thousand so-called power cycles. In this particular case, the microelectronic chip in the BGA serves as a heat source and leads to accelerated aging of the solder as follows.

The regions of different shades of gray and black indicate that the originally fine mix between tin and lead is superseded by islands of high lead and tin concentrations. These form as a result of a diffusion-driven separation of both phases known as coarsening. Experiments have shown that diffusion processes can be considerably accelerated by combination of relatively high temperatures ($>80^{\circ}C$) in combination with mechanical stresses (cf., e.g., Ozmat, 1990; Harris et al., 1991; Hacke et al., 1991; Pao, 1992; Nylén, 1997). Consequently, the overall material properties of the solder change over time which, eventually, will

have a detrimental effect on the mechanical stability of the joint. Furthermore, note that cracks have formed at the upper and lower boundaries of the solder bump where, due to diffusion from the adjacent copper and nickel layers, intermetallics have been formed, which are quite susceptible to brittle fracture.

It is the intention of this paper to present a suitable theoretical framework that allows to quantitatively assess the coarsening process in *binary* alloys. It will specifically be applied to study phase separation in eutectic SnPb solders. However, it should be noted that it is automatically applicable to other binaries, provided that all the necessary material parameters are known. As will be shown, all of these parameters are *physically based* and obtainable from measurements independent of the coarsening phenomenon. In other words, there is no need for artificial adjustment in order to fit the experimental observations on coarsening that are of specific interest to this paper.

It should be possible to extend the presented theory to ternary or quartenary systems. However, depending on the number of components, the quantitative evaluation of the resulting system of diffusion equations would certainly require specific knowledge of many additional material parameters. Very likely, these will not easily be obtainable and, surely, the complexity of the numerical difficulties encountered during solution of the corresponding partial differential equations will also increase.

Nevertheless, it is fair to say that the theory presented in this paper provides a quantitative tool and may serve as guidance during the selection and assessment process regarding the suitability of lead-free solders in microelectronic applications. Due to environmental constraints, [2] the fatigue and aging properties of such systems such as SnAg, SnCu, SnSb, SnAgCu, SnAgCuBi, SnAgCuSb, etc. have been the recent focus of attention (cf., Lee, 1997; Lord et al., 1997). Some of these new solder materials are known to show similar coarsening characteristics as SnPb (see Chada et al., 1997 for the case of SnAg). Consequently, a tractable theory in combination with suitable experiments may help to ease the concerns of the industry during the upcoming transition period as far as reliability issues are concerned.

1.2. Extended diffusion equations and phase field models

In a recent paper, Dreyer and Müller (2000) presented an extended diffusion equation and modeled the phase separation and coarsening processes observed in binary tin lead solders that are subjected to thermomechanical loads. The equation reads:

$$\rho_0 \frac{\partial c}{\partial t} + \frac{\partial J_i}{\partial x_i} = 0, \tag{1.1}$$

and contains an "extended" diffusion flux, J_i, as follows:

$$J_i = -\rho_0 M_{ij} \frac{\partial}{\partial x_j} \left(\frac{\partial \psi}{\partial c} - a_{kl} \frac{\partial^2 c}{\partial x_k \partial x_l} + \frac{\partial}{\partial c} \left[\frac{1}{2} \left(\varepsilon_{kl} - \varepsilon^*_{kl} \right) C_{klrs} \left(\varepsilon_{rs} - \varepsilon^*_{rs} \right) \right] \right). \tag{1.2}$$

The adjective "extended" refers to the fact that within the scope of this theory, classical diffusion of the Fickian type (the first term in the parentheses), effects of surface tension according to the Cahn–Hilliard formalism (second term, Cahn and Hilliard, 1958), as well as the influence of stresses and strains (third term) on diffusional morphology changes are taken into account. More specifically, the meaning of all symbols used in the equation is

[2] Various bills have recently been introduced at the US congress (Lau and Chang, 1999) to ban lead from a variety of uses including solders and, similarly, the EC is strongly promoting lead-free soldering as part of its campaign for recycling and waste storage of electronic products (Low and Williams, 1998).

- ρ_0: total mass density of the alloy with respect to the reference configuration, i.e., a constant;
- $c = \tilde{c}(\underline{x}, t)$: distribution of the mass concentration of tin as a function of positions, $\underline{x}$, and time, t, which originally is defined as follows ($\tilde{\rho}^{\mathrm{Sn}}(\underline{x}, t)$ is the mass density of the tin, m^{Sn} is the mass of the tin and m, the total mass of the alloy within a small material element at position $\underline{x}$ and time t):

$$c = \tilde{c}(x_k, t) = \frac{\tilde{\rho}^{\mathrm{Sn}}(x_k, t)}{\rho_0} = \frac{m^{\mathrm{Sn}}}{m}. \tag{1.3}$$

- $M_{ij} = \widetilde{M}_{ij}(\underline{x}, t)$: the mobility matrix, which will be related to the (constant) mobilities, $M_{ij}^{\alpha/\beta}$ of the α and of the β-phase as follows:

$$M_{ij} = \tilde{\theta}(\underline{x}, t) M_{ij}^{\alpha} + (1 - \tilde{\theta}(\underline{x}, t)) M_{ij}^{\beta}, \tag{1.4}$$

where the shape function, $\tilde{\theta}(\underline{x}, t)$, of Eq. (1.4) is defined by

$$\theta = \tilde{\theta}(\underline{x}, t) = \frac{c^{\beta} - \tilde{c}(\underline{x}, t)}{c^{\beta} - c^{\alpha}} \Rightarrow \theta(\underline{x}, t) = \begin{cases} 0 & \text{if } \underline{x} \in \beta, \\ 1 & \text{if } \underline{x} \in \alpha, \end{cases} \tag{1.5}$$

c^{α} and c^{β} being the equilibrium concentrations of tin in the lead- and in the tin-rich phase, respectively.

- ψ: the configurational part of the Gibbs free energy density of the system (in $\mathrm{J\,m^{-3}}$), which in the paper by Dreyer and Müller (2000) was assumed in form of a fourth order Landau polynomial, and ψ_0 being another numerical constant, which in their work was used for normalization purposes:

$$\psi = \widetilde{\psi}(c) = \psi_0 \left(\left([c^{\alpha} - c_0]^2 - [c - c_0]^2 \right)^2 \right), \quad c_0 = \tfrac{1}{2}\left(c^{\alpha} + c^{\beta}\right). \tag{1.6}$$

In order to study the influence of "low" and "high" temperatures, the following data was originally chosen:

$$T_{\mathrm{high}} = 150^{\circ}\mathrm{C}: \quad c^{\alpha} = 11.88\%, \quad c^{\beta} = 97.98\%, \tag{1.7}$$

$$T_{\mathrm{low}} = 20^{\circ}\mathrm{C}: \quad c^{\alpha} = 1.54\%, \quad c^{\beta} = 99.86\%. \tag{1.8}$$

The corresponding free energy plots are shown in Fig. 3 (after normalization with ψ_0). Note that the bump separating the two phase equilibria [3] increases with a decreasing temperature. Suggestively speaking, we may want to interpret this as a higher barrier that needs to be overcome during the phase separation process and which should correspond to a higher level of stability, i.e., increase of the duration of the phase separation process.

- a_{ij}: a matrix containing surface tension related quantities of both phases ($a_{kl}^{\alpha/\beta}$ being constants):

$$a_{kl} = \tilde{\theta}(\underline{x}, t) a_{kl}^{\alpha} + (1 - \tilde{\theta}(\underline{x}, t)) a_{kl}^{\beta}; \tag{1.9}$$

- ε_{ij}: the total strains;
- ε_{kl}^{*}: the eigenstrains resulting from different thermal expansion of the two phases ($\alpha_{kl}^{\alpha/\beta}$ being the thermal expansion coefficients of both phases, T the current temperature, and T_{R} being the temperature stress free state of reference):

$$\varepsilon_{kl}^{*} = \tilde{\alpha}_{kl}(\underline{x}, t) \cdot \Delta T, \quad \Delta T = (T - T_{\mathrm{R}}), \quad \alpha_{kl} = \tilde{\theta}(\underline{x}, t) \alpha_{kl}^{\alpha} + (1 - \tilde{\theta}(\underline{x}, t)) \alpha_{kl}^{\beta}; \tag{1.10}$$

- C_{ijkl}: the local stiffness to be obtained from the stiffnesses of both phases, $C_{ijkl}^{\alpha/\beta}$:

$$C_{ijkl} = \tilde{\theta}(\underline{x}, t) C_{ijkl}^{\alpha} + (1 - \tilde{\theta}(\underline{x}, t)) C_{ijkl}^{\beta}. \tag{1.11}$$

[3] These are indicated by the two dots.

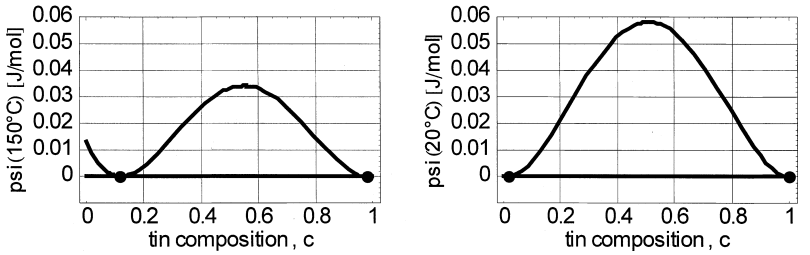

Fig. 3. Free energy curves of the SnPb system from a fourth order Landau polynomial (high temperature left, low temperature right) including Maxwell tangent construction.

The comparison between simulations and experiments shown in Fig. 4 demonstrates the ability of this theory to describe the coarsening process observed in eutectic SnPb solders. The first two rows refer to experiments (Harris et al., 1991) that prove the effect of room temperature aging after (a) 2 h, (b) 17 days, and (c) 63 days after solidification; bottom row: (a) immediately after solidification, (b) after 3 h and (c) 300 h at 125°C. The last two rows show the corresponding development of the coarsening at low and high temperatures, respectively, as predicted by computer simulations (Dreyer and Müller, 2000). It should be pointed out that the computer simulations of SnPb coarsening in that paper were purely *qualitative*. At the time when they were performed, numerical data for two important material parameters was not known to the authors, namely the Gibbs free energy of the alloy and the mobility coefficients of the atom species that participate in the diffusion process. We proceed to investigate this in more detail in the following section.

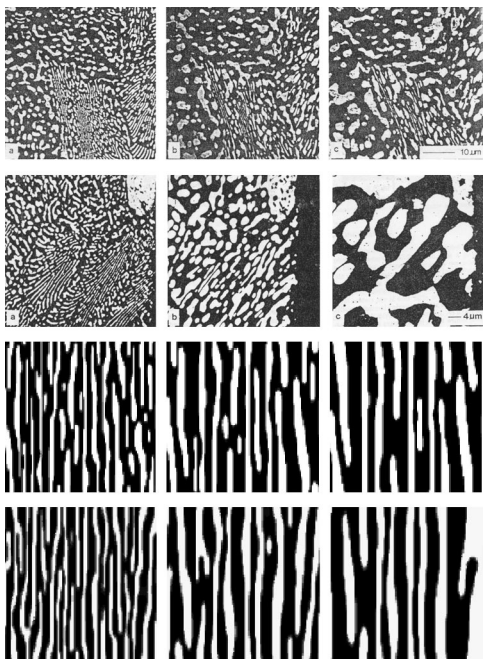

Fig. 4. Comparisons of the coarsening process in SnPb solders: experimental observations vs. computer simulations (see text).

In particular, in order to allow for a direct comparison between the experimental results presented in Harris et al. (1991), we will choose the high temperature state to be $T_{\text{high}} = 125°\text{C}$ from now on.

2. Materials science aspects

The first two of the following subsections concentrate on the material parameters that were insufficiently known in the previous paper by the authors. The third subsection summarizes all the other relevant data.

2.1. The Gibbs free energy

Following the MTData® report (1998), the Gibbs free energy densities (in units of J mol^{-1}) for a binary system A/B can be obtained for both phases individually as a function of particle concentrations, y:

$$g^{\alpha/\beta} = \tilde{g}^{\alpha/\beta}(y) = y g_A^{\alpha/\beta} + (1-y) g_B^{\alpha/\beta} + RT[y \ln(y) + (1-y)\ln(1-y)] + y(1-y) l_{A,B}^{\alpha}, \tag{2.1}$$

where the particle concentration is defined by (N^{Sn} is the number of tin particles and N, the total number of particles within the material volume element at position $\underline{x}$ and time t)

$$y = \tilde{y}(x_k, t) = \frac{N^{\text{Sn}}}{N}. \tag{2.2}$$

The symbols $g_A^{\alpha/\beta}$, $g_B^{\alpha/\beta}$, $l_{A,B}^{\alpha}$ depend on absolute temperature, T, and were obtained from fits to experimental data as follows:

$$g_j^i = A_j^i + B_j^i T + C_j^i T \ln(T) + D_j^i T^2 + E_j^i T^3 + \frac{F_j^i}{T}, \quad i \in \{\alpha, \beta\}, \quad j \in \{A, B\}, \tag{2.3}$$

$$l_{A,B}^i = A^i + B^i T, \quad i \in \{\alpha, \beta\}. \tag{2.4}$$

More specifically, for the SnPb system with

$$A = \text{Sn}, \qquad B = \text{Pb}. \tag{2.5}$$

MTData® provides the following numerical values valid within the temperature range $250\ \text{K} < T < 505\ \text{K}$:

	A_j^i (kJ mol^{-1})	B_j^i (J mol^{-1})	C_j^i $(\text{J mol}^{-1}\,\text{K}^{-1})$	D_j^i $(\text{mJ mol}^{-1}\,\text{K}^{-2})$	E_j^i $(\mu\text{J mol}^{-1}\,\text{K}^{-3})$	F_j^i (MJ K mol^{-1})
$i = \alpha$						
$j = \text{Pb}$	−7.650085	101.700244	−24.524223	−3.65895	−0.24395	0
$j = \text{Sn}$	−1.705135	60.2433150	−15.9610	−18.8702	3.121167	−0.06196
$i = \beta$						
$j = \text{Pb}$	−7.161085	105.220244	$= C_{\text{Pb}}^{\alpha}$	$= D_{\text{Pb}}^{\alpha}$	$= E_{\text{Pb}}^{\alpha}$	$= F_{\text{Pb}}^{\alpha}$
$j = \text{Sn}$	−5.855135	65.4433150	$= C_{\text{Sn}}^{\alpha}$	$= D_{\text{Sn}}^{\alpha}$	$= E_{\text{Sn}}^{\alpha}$	$= F_{\text{Sn}}^{\alpha}$

	A^i (kJ mol^{-1})	B^i (J mol^{-1})
$i = \alpha$	5.13241	1.56312
$i = \beta$	17.11778	−11.80656

The result is shown in Fig. 5, for the following choice of high and low temperature equilibrium states:

$$T_{\text{high}} = 125°\text{C}: \quad y^{\alpha} = 15.00\%, \quad y^{\beta} = 98.76\%, \tag{2.6}$$

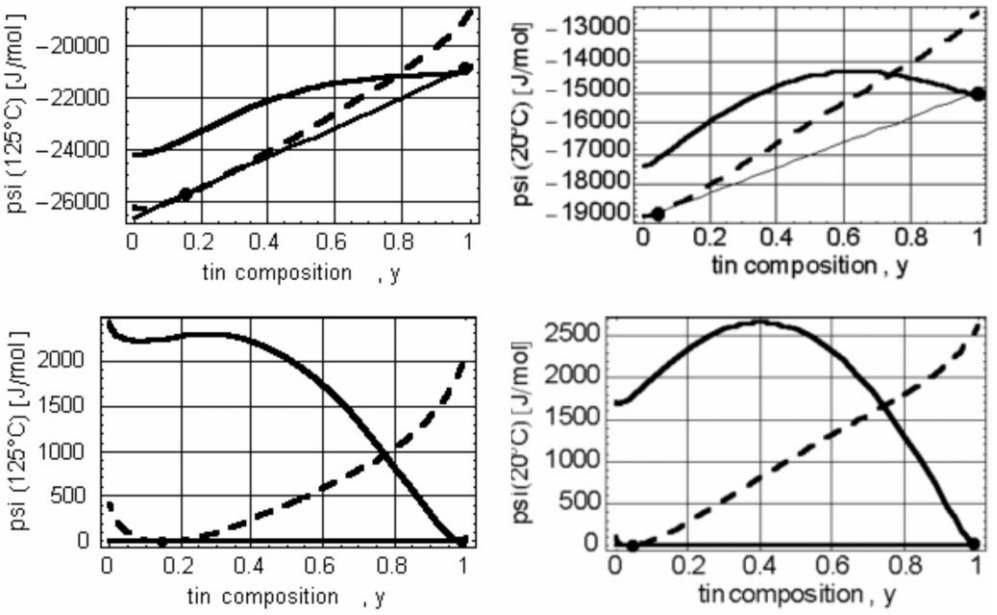

Fig. 5. Top row: free energy curves of the SnPb system from MTData® (high temperature left, low temperature right, dashed and solid curves refer to the α and to the β-phase, respectively) including Maxwell tangent construction; bottom row: situation after deduction of Maxwell line from free energy curves.

$$T_{\text{low}} = 20^{\circ}\text{C}: \quad y^{\alpha} = 4.12\%, \quad y^{\beta} = 99.81\%. \tag{2.7}$$

It is important to note that the MTData® report provided two sets of Gibbs free energy curves, i.e., one for each phase, and that in the report they were both plotted for the full range of concentrations, $0 \leqslant y \leqslant 1$ at 300 and 450 K. Just as in Fig. 5, both curves showed a non-convex behavior similar to the one for the single phenomenological free energy curve shown in Fig. 3.

On first glance, this is slightly confusing since one might conclude that four equilibrium concentrations will result. However, this is not so. Rather, the Maxwell construction must be performed such that the common tangent touches the free energy of the α-phase on the left, i.e., at low concentrations, and the free energy curve of the β-phase on the right, i.e., at high concentrations (see the Maxwell tangent lines in Fig. 5, top row).

Moreover, as required within the framework of our theory, a single free energy distribution for SnPb valid over the full range of concentrations $0 \leqslant y \leqslant 1$ can be obtained by taking the lower energy level of the free energy curves of the α and of the β phase, respectively. Obviously, if a common tangent construction is now applied to this single curve, the resulting equilibrium concentrations are identical with those obtained before.

The second row of plots in Fig. 5 follows from the first row by subtraction of the common tangent from the free energy curves for the two phases. This was done to allow for a direct comparison to the Landau polynomial shown in Fig. 3 and Eq. (1.6). Note that if the common free energy curve in these two plots is considered (to be constructed as outlined above), the low temperature curve will show a higher bump (at the kink) than the high temperature curve despite the fact that the dependence is shown as a function of y, i.e., particle concentrations instead of mass concentrations, c. In fact, this behavior is *independent* of the choice of concentrations as we shall see now.

Recall that the theory that led to the extended diffusion equations presented in Section 1.2 was originally developed in terms of mass concentrations, c, and not in particle concentrations, y. In order to avoid its complete reformulation, it is easier to rewrite the Gibbs free energy densities instead. In order to perform the switch from particle to mass concentrations, we argue as follows ($\mu_H = 1.675 \times 10^{-24}$ kg denotes the mass of one hydrogen atom, $M^{Sn} = 118.69$ and $M^{Pb} = 207.19$ are the atomic weights of tin and lead, respectively, particle and mass conservation is observed):

$$m^{Sn} = M^{Sn} N^{Sn} \mu_H, \qquad m = \left(M^{Sn} N^{Sn} + M^{Pb}\left(N - N^{Sn}\right)\right)\mu_H. \tag{2.8}$$

Inserting this into the definitions shown in Eqs. (1.3) and (2.2) yields

$$y = \tilde{y}(c) = \frac{M^{Pb} c}{M^{Sn} - c(M^{Sn} - M^{Pb})} \Longleftrightarrow c = \tilde{c}(y) = \frac{M^{Sn} y}{M^{Pb} - y(M^{Pb} - M^{Sn})}. \tag{2.9a, b}$$

This *non-linear* relationship must be inserted into Eqs. (2.1)–(2.3) in order to obtain the free energy curves suitable for the diffusion equation shown in Eqs. (1.1) and (1.2). Note that the non-linearity of the free energy function changes during the switch in variables. For example, terms that were formerly linear in particle concentrations y and $(1 - y)$, become non-linear when Eq. (2.9a) is inserted. Specifically, at the two temperatures, we obtain:

$$T_{high} = 125^\circ C: \quad c^\alpha = 9.18\%, \quad c^\beta = 97.86\%, \tag{2.10}$$

$$T_{low} = 20^\circ C: \quad c^\alpha = 2.40\%, \quad c^\beta = 99.67\%. \tag{2.11}$$

Moreover, in order to convert the free energy densities from $J\,mol^{-1}$ into $J\,m^{-3}$, it is useful to introduce an average molecular weight, $M = \widetilde{M}(c)$, which changes as a function of concentration. To this end, we start with the equation for mass conservation for a material volume element at position $\underline{x}$ and time t:

$$M \cdot N \cdot \mu_H = \left(M^{Sn} \cdot N^{Sn} + \left(N - N^{Sn}\right)M^{Pb}\right) \cdot \mu_H \Rightarrow \widetilde{M}(c) = \tilde{y}(c) M^{Sn} + (1 - \tilde{y}(c)) M^{Pb}, \tag{2.12}$$

where the definition from Eq. (2.2) and the fact that particle numbers are conserved has been used. If Eq. (2.9a) is inserted into this relation, we find that:

$$M = \widetilde{M}(c) = \frac{M^{Pb} M^{Sn}}{M^{Sn} - c(M^{Sn} - M^{Pb})}. \tag{2.13}$$

By means of Avagadro's number, $N_{Avo} = 6.0225 \times 10^{23}\ mol^{-1}$, we may write:

$$N_{Avo} \cdot \mu_H = 6.0225 \times 10^{23}\ mol^{-1} \cdot 1.675 \times 10^{-27}\ kg = 10^{-3}\ kg\,mol^{-1}. \tag{2.14}$$

This in combination with Eqs. (2.9a,b), (2.13), and (2.1) can now be used to establish experimentally based specific free energies, $\psi^{\alpha/\beta}$, which (after multiplication by the macroscopic density of the eutectic alloy, $\rho(SnPb) = c_{eut}\rho(Sn) + (1 - c_{eut})\rho(Pb) \approx 8800\ kg\,m^{-3}$, where $c_{eut} = 0.619$, $\rho(Sn) \approx 7260\ kg\,m^{-3}$, and $\rho(Pb) \approx 11\,300\ kg\,m^{-3}$, and suitable combination to form a single differentiable function) can directly be used for numerical evaluation of the extended diffusion equation shown in Eqs. (1.1)–(1.2):

$$\psi^{\alpha/\beta} = \tilde{\psi}^{\alpha/\beta}(c) = \frac{\tilde{g}^{\alpha/\beta}(\tilde{c}(y))}{\widetilde{M}(c)} \times 10^3\ mol\,kg^{-1}. \tag{2.15}$$

The result of this procedure is presented in Fig. 6, which is to be understood analogously to the sequence of plots shown in Fig. 3. It seems worth mentioning that the mass concentrations obtained from the common tangent construction performed with the curves from Fig. 6 agrees with the equilibrium particle concen-

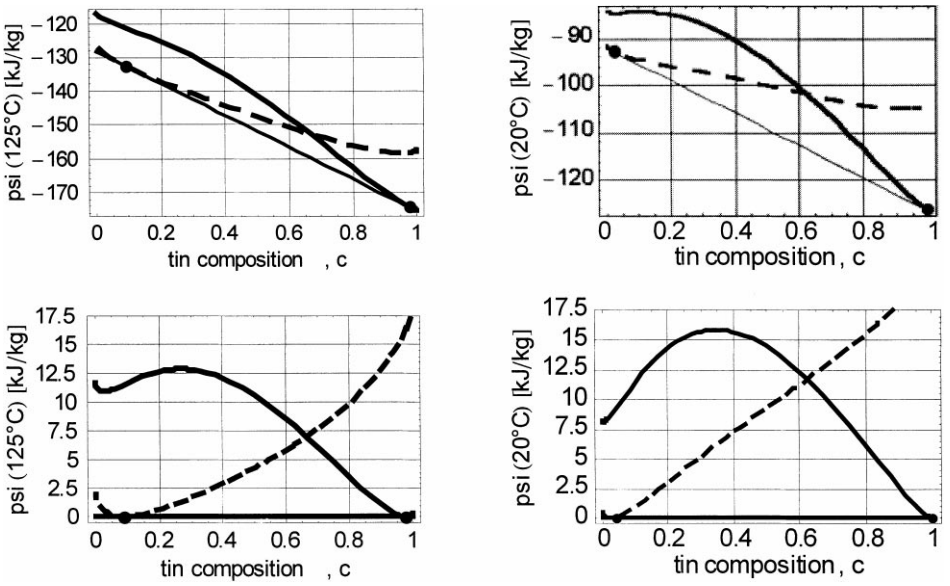

Fig. 6. Top row: Free energy curves of the SnPb system from MTData® (high temperature left, low temperature right, dashed and solid curves refer to the α and to the β-phase, respectively) including Maxwell tangent construction; bottom row: situation after deduction of Maxwell line from free energy curves.

trations from Fig. 5 after the latter have been converted into mass concentrations by means of Eq. (2.9b). Note that the numerator in Eq. (2.15) is crucial to achieve this agreement.

It was indicated before that within the theory presented in this paper, a *single* free energy function is required for the full range of concentrations that can be obtained by choosing the lower energy level of the free energy curves of the α and of the β phase, respectively. However, note that the resulting function will show a kink at the cross-over point between the free energies for the two phases. This is of a great disadvantage during the numerical analysis (which requires continuous first- and second-order derivatives of the free energy as we will describe in Sections 2.2, 3.2, and 3.3). Therefore, a seventh-order polynomial in concentration was used for a curve fit of the non-convex region. The required eight constants of this polynomial were determined such that the free energy is continuously differentiable up to second-order. By doing this, it was also made certain that the spinodal concentrations (if determined from the requirement of vanishing second-order derivatives) were properly recovered. The final result is presented in Fig. 7.

Finally, it should be mentioned that the Gibbs free energy curves of MTData® stem from experiments performed with macroscopic specimens. They were not obtained from microscopic studies of local equilibrium between the phases of an alloy. Nevertheless, we will use these global Gibbs free energies to study local equilibrium using *locally* valid equations, e.g., Eqs. (1.1)–(1.2). This is certainly an extrapolation of the original range of validity of experiments. However, as we shall see, the numerical predictions on coarsening that are based on this extrapolation agree fairly well with microstructural observations.

2.2. Diffusion constants

In Dreyer and Müller (2000), it was assumed that the symmetry of a phase is determined by the symmetry of the dominant constituent. In other words, the α-phase was assumed as cubic (as in lead) and the β-phase as tetragonal (as in tin). Following up on Eq. (1.4), we therefore write (provided the axes of the crystal and of the laboratory frame coincide):

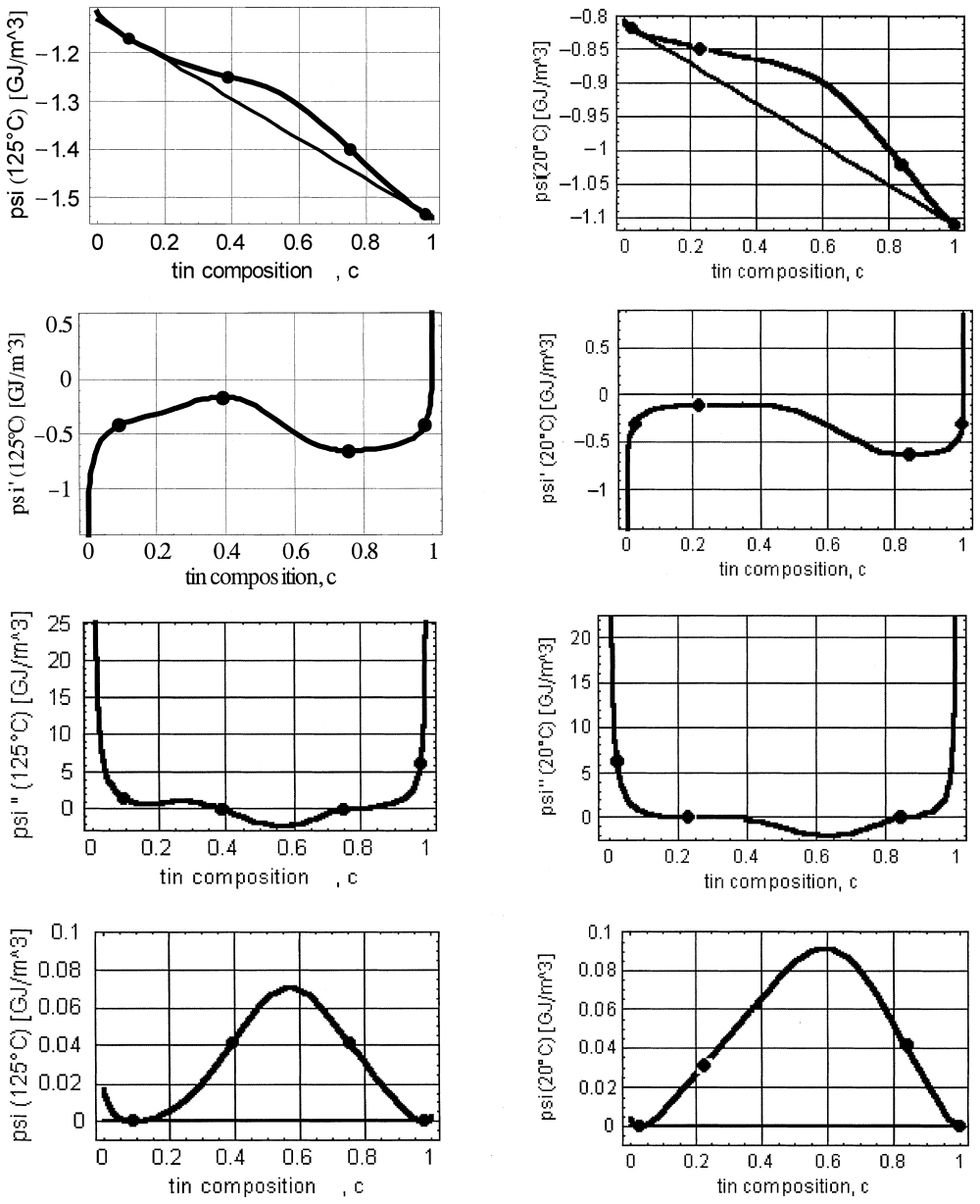

Fig. 7. Joint Gibbs free energy curves, first and second derivative of the SnPb system derived from MTData® (high temperature left, low temperature right) including Maxwell concentrations (outermost points) and spinodal concentrations (innermost points); fourth row: free energies after deduction of the Maxwell line.

$$M^{\alpha}_{ij} = M^{\alpha}\delta_{ij}, \qquad M^{\beta}_{ij} = \begin{pmatrix} M^{\beta}_{1} & 0 & 0 \\ 0 & M^{\beta}_{1} & 0 \\ 0 & 0 & M^{\beta}_{3} \end{pmatrix}. \tag{2.16}$$

In these equations, M^{α} and $M^{\beta}_{1,3}$ denote the mobilities of tin atoms in a lead dominated lattice and of lead atoms in a tin dominated crystal, respectively. To the best knowledge of the authors, these material co-

efficients are not directly available in the literature. Therefore, we follow an argument outlined by Küpper and Masbaum (1994) and attempt to relate the mobility coefficients to diffusion coefficients. To this end, we concentrate on diffusion of the Fickean type and write:

$$J_i \sim -\rho_0 M_{ij} \frac{\partial}{\partial x_j}\left(\frac{\partial \psi(c)}{\partial c}\right) = -\rho_0 M_{ij} \frac{\partial^2 \psi(c)}{\partial c^2} \frac{\partial c}{\partial x_j} = -\rho_0 D_{ij} \frac{\partial c}{\partial x_j}, \tag{2.17}$$

where after the last equality sign the matrix of the coefficients of diffusion has been defined, D_{ij}. We conclude that mobilities and diffusion coefficients are related to each other as follows:

$$D_{ij} = M_{ij} \frac{\partial^2 \psi}{\partial c^2}, \qquad D_{ij} = \tilde{\theta}(\underline{x}, t) D_{ij}^{\alpha} + (1 - \tilde{\theta}(\underline{x}, t)) D_{ij}^{\beta}. \tag{2.18a, b}$$

Küpper and Masbaum evaluated the second derivative of the Gibbs free energy density for a concentration in the metastable area of the miscibility gap, e.g., for the eutectic concentration that was used by Dreyer and Müller (2000) as the initial condition. However, in order to assess mobilities relevant to the long-term structural development, when the structure gets closer and closer to equilibrium, it seems more reasonable to evaluate Eq. (2.18a) for the equilibrium concentrations, c^{α} and c^{β}, depending on whether the mobilities in the lead- or tin-rich phase are of interest. The meaning of the symbols $D_{ij}^{\alpha/\beta}$ is analogous to that of $M_{ij}^{\alpha/\beta}$. Consequently, information regarding the following data is finally required:

$$D_{ij}^{\alpha} = D^{\alpha} \delta_{ij}, \qquad D_{ij}^{\beta} = \begin{pmatrix} D_1^{\beta} & 0 & 0 \\ 0 & D_1^{\beta} & 0 \\ 0 & 0 & D_3^{\beta} \end{pmatrix}. \tag{2.19a, b}$$

Tracer impurity diffusion coefficients of tin in (pure) lead and lead in (pure) tin have been reported in the literature (see Decker et al., 1977; Sen and Ghorai, 1989 (which contains further references); Ghosh and Liu, 1998). According to these references, an Arrhenius relationship can be established as follows:

$$D^{\alpha} = D^{\alpha 0} \exp\left[-\frac{Q^{\alpha 0}}{kT}\right], \qquad D_1^{\beta} = D_3^{\beta} = D^{\beta 0} \exp\left[-\frac{Q^{\beta 0}}{kT}\right], \tag{2.20}$$

where $k = 1.38 \times 10^{-23}\ \mathrm{J\,K^{-1}} = 0.8617 \times 10^{-4}\ \mathrm{eV\,K^{-1}}$ denotes Boltzmann's constant. The remaining parameters are given by [4]:

$$D^{\alpha 0} = 4.1 \times 10^{-5}\ \mathrm{m^2\,s^{-1}}, \qquad Q^{\alpha 0} = 1.03\ \mathrm{eV}, \tag{2.21}$$

$$D^{\beta 0} = 3.533 \times 10^{-6}\ \mathrm{m^2\,s^{-1}}, \qquad Q^{\beta 0} = 0.64\ \mathrm{eV}. \tag{2.22}$$

By doing this, it was assumed that diffusion coefficients for tracer impurities can still be used in a situation where the percentage of the diffusing species in the overall alloy constitution is no longer insignificant (cf., Eqs. (2.6) and (2.7)). Indeed, by looking at Fig. 3 from the work of Oberschmidt et al. (1982), we must conclude that there will certainly be an influence of the tin concentration in the dispersing alloy on the diffusion coefficient. However, to detect a trend is by no means obvious since the curve for the tracer diffusion coefficient in that figure falls in between the curves for lead that contains 3% and 9% tin. Therefore, during our simulations, we shall simply use the diffusion coefficient for tin or lead being a tracer element in pure lead and tin. It should also be pointed out that the coefficients shown in Eqs. (2.21) and (2.22) hold within a temperature range of $240 - 325^{\circ}\mathrm{C}$ and $195 - 322^{\circ}\mathrm{C}$, respectively. This should be kept in mind when using them at $125^{\circ}\mathrm{C}$ or $20^{\circ}\mathrm{C}$.

[4] The first datum stems from Decker et al. (1977), Sen and Ghorai (1989) report a slightly different value which was not used in our simulations: $D^{\alpha 0} = 2.9 \times 10^{-5}\ \mathrm{m^2\,s^{-1}}$.

Moreover, it seems noteworthy that (Ghosh and Liu, 1998) report *no* effect of anisotropy, i.e., $D_1^\beta = D_3^\beta$ for the diffusion of lead tracer atoms in tin. This seems slightly curious since for many other tracer elements in tin such an effect has been demonstrated. For example, as shown in Table 13.2 of the data handbook edited by Brandes (1983), zinc diffuses at a ratio of $D_1 : D_3 = 764 : 1$. Other elements, such as mercury (which by its atomic size and weight is comparable to lead) show a much lesser degree of anisotropy, $D_1 : D_3 = 4 : 1$. Ghosh and Liu also present isotropic data for the self-diffusion of tin and indium, whereas the data by Brandes clearly indicates (slightly) different self-diffusion coefficients in the two main directions. Therefore, we will interpret Ghosh and Liu's data with a caveat but use them to find the right order of magnitude for the diffusion as well as the mobility coefficients.

In fact, by using their data, it turns out that diffusion within the tin-rich regions is considerably faster than in the lead-rich regions. If Eqs. (2.21) and (2.22) are inserted into Eq. (2.20), the following data for the diffusion coefficients are obtained:

$$125^\circ\mathrm{C}: \quad D^\alpha = 3.71 \times 10^{-18}\ \mathrm{m^2\,s^{-1}}, \quad D_1^\beta = D_3^\beta = 2.78 \times 10^{-14}\ \mathrm{m^2\,s^{-1}}, \tag{2.23a, b}$$

$$20^\circ\mathrm{C}: \quad D^\alpha = 7.86 \times 10^{-23}\ \mathrm{m^2\,s^{-1}}, \quad D_1^\beta = D_3^\beta = 3.46 \times 10^{-17}\ \mathrm{m^2\,s^{-1}}, \tag{2.24}$$

which, by virtue of Eq. (2.18a,b), results in the following mobility data:

$$125^\circ\mathrm{C}: \quad M^\alpha|_{c^\alpha} = 2.42 \times 10^{-27}\ \mathrm{m^5\,J^{-1}s^{-1}}, \quad M_1^\beta\big|_{c^\beta} = M_3^\beta\big|_{c^\beta} = 4.52 \times 10^{-24}\ \mathrm{m^5\,J^{-1}s^{-1}}, \tag{2.25}$$

$$20^\circ\mathrm{C}: \quad M^\alpha|_{c^\alpha} = 1.27 \times 10^{-32}\ \mathrm{m^5\,J^{-1}s^{-1}}, \quad M_1^\beta\big|_{c^\beta} = M_3^\beta\big|_{c^\beta} = 1.11 \times 10^{-27}\ \mathrm{m^5\,J^{-1}s^{-1}}. \tag{2.26}$$

2.3. Miscellaneous material data

For the surface tension related quantities relevant in Eq. (1.9), data presented in the paper by Dreyer and Müller (2000) were used (γ denotes the surface energy, Δx is the width of the interface):

$$a = \frac{2\gamma\Delta x}{(c^\beta - c^\alpha)^2}, \quad \gamma = 1.5\ \mathrm{J\,m^{-2}}, \quad \Delta x = 25\ \mathrm{nm}, \tag{2.27}$$

$$a_{kl}^\alpha = a^\alpha \delta_{ij}, \qquad a^\alpha = 1.5 \times a, \qquad a_{kl}^\beta = \begin{pmatrix} a & 0 & 0 \\ 0 & a & 0 \\ 0 & 0 & 14a \end{pmatrix}. \tag{2.28}$$

It should be pointed out that the anisotropy of surface tensions of the β-phase was used in the paper by Dreyer and Müller (2000) to explain and simulate the formation of lamella-type structures and directional coarsening in eutectic SnPb solders. Also note that, alternatively or in addition to this, differences in the diffusion coefficients of the β-phase could be used to explain directional coarsening, Eq. (2.19b). However, so far there is no experimental support for this (cf., Eq. (2.23b)), and, in addition, a quantitative discussion of such an effect is a priori beyond the scope of the *one-dimensional* simulations discussed in this paper and will be left to future research.

Thermal as well as elastic coefficients can be obtained from (see Dreyer and Müller, 2000, for all relevant references):

$$\alpha_{ij}^\alpha = \begin{pmatrix} \alpha^\alpha & 0 & 0 \\ 0 & \alpha^\alpha & 0 \\ 0 & 0 & \alpha^\alpha \end{pmatrix}, \qquad \alpha_{ij}^\beta = \begin{pmatrix} \alpha_1^\beta & 0 & 0 \\ 0 & \alpha_1^\beta & 0 \\ 0 & 0 & \alpha_3^\beta \end{pmatrix}, \tag{2.29}$$

$$\alpha^\alpha = 28.9 \times 10^{-6}\ \mathrm{K^{-1}}, \qquad \alpha_1^\beta = 16.7 \times 10^{-6}\ \mathrm{K^{-1}}, \qquad \alpha_3^\beta = 36.4 \times 10^{-6}\ \mathrm{K^{-1}}, \tag{2.30}$$

and:

kl / ij	11	22	33	23	31	12
11	C^{α}_{11}	C^{α}_{12}	C^{α}_{12}	0	0	0
22	C^{α}_{12}	C^{α}_{11}	C^{α}_{12}	0	0	0
33	C^{α}_{12}	C^{α}_{12}	C^{α}_{11}	0	0	0
23	0	0	0	C^{α}_{44}	0	0
31	0	0	0	0	C^{α}_{44}	0
12	0	0	0	0	0	C^{α}_{44}

,

kl / ij	11	22	33	23	31	12
11	C^{β}_{11}	C^{β}_{12}	C^{β}_{13}	0	0	0
22	C^{β}_{12}	C^{β}_{11}	C^{β}_{13}	0	0	0
33	C^{β}_{13}	C^{β}_{13}	C^{β}_{33}	0	0	0
23	0	0	0	C^{β}_{44}	0	0
31	0	0	0	0	C^{β}_{44}	0
12	0	0	0	0	0	C^{β}_{66}

, (2.31)

$$C^{\alpha}_{11} = 49.66 \text{ GPa}, \qquad C^{\alpha}_{12} = 42.31 \text{ GPa}, \qquad C^{\alpha}_{44} = 14.98 \text{ GPa}, \tag{2.32}$$

$$C^{\beta}_{11} = 75.29 \text{ GPa}, \qquad C^{\beta}_{12} = 61.56 \text{ GPa}, \qquad C^{\beta}_{13} = 44.00 \text{ GPa},$$

$$C^{\beta}_{33} = 95.52 \text{ GPa}, \qquad C^{\beta}_{44} = 21.93 \text{ GPa}, \qquad C^{\beta}_{66} = 23.36 \text{ GPa}. \tag{2.33}$$

To reduce the numerical effort, only 1D simulations will be presented in this paper. Consequently, the Representative Volume Element (RVE) becomes a line which was identified with the 1-axis and chosen to be of a length $2\pi L = 1$ μm.

3. Mathematical aspects

3.1. Solution of the mechanical problem in 1D

We consider deformation in only one-dimension, $x = x_1$, i.e.

$$\varepsilon_{11} = \varepsilon = \tilde{\varepsilon}(x,t) \tag{3.1}$$

is the only non-vanishing component of the strain tensor, ε_{ij}, and

$$\varepsilon^{*}_{11} = \varepsilon^{*} = \tilde{\varepsilon}^{*}(x,t) = \alpha^{\beta}_{1} - \theta \cdot \left(\alpha^{\beta}_{1} - \alpha^{\alpha}\right), \qquad \theta = \tilde{\theta}(x,t) = \frac{c^{\beta} - c}{c^{\beta} - c^{\alpha}}, \quad c = \tilde{c}(x,t) \tag{3.2}$$

is the only component for the eigenstrains. Under these circumstances (also see Eq. (2.31)) Hooke's law implies:

$$\sigma_{11} = \left(C^{\beta}_{11} - \theta \cdot \left(C^{\beta}_{11} - C^{\alpha}_{11}\right)\right) \cdot (\varepsilon - \varepsilon^{*}), \tag{3.3a}$$

$$\sigma_{22} = \left(C^{\beta}_{12} - \theta \cdot \left(C^{\beta}_{12} - C^{\alpha}_{12}\right)\right) \cdot (\varepsilon - \varepsilon^{*}), \tag{3.3b}$$

$$\sigma_{33} = \left(C^{\beta}_{13} - \theta \cdot \left(C^{\beta}_{13} - C^{\alpha}_{12}\right)\right) \cdot (\varepsilon - \varepsilon^{*}), \tag{3.3c}$$

$$\sigma_{13} = 0, \qquad \sigma_{23} = 0, \qquad \sigma_{12} = 0. \tag{3.3d}$$

The second and the third equation must be interpreted as a stress constraint, similarly to the one imposed on the third dimension, if a material is required to stay in a state of plane strain.

Moreover, the equation for static equilibrium of forces has to be observed:

$$\frac{\partial \sigma_{ij}}{\partial x_j} = 0. \tag{3.4}$$

By virtue of Eqs. (3.1)–(3.3a–d) the only non-vanishing component reads:

$$\frac{\partial \sigma_{11}}{\partial x} = 0, \tag{3.5}$$

which implies that σ_{11} must be a constant with respect to space:

$$\sigma_{11} = \sigma_0 = \text{const.}_x. \tag{3.6}$$

In fact, σ_0 is nothing else but the external stress applied to the ends of a 1D rod made of solder. Physically speaking, we may interpret this stress as an external load that stems from the load imposed on a solder joint because the to-be-joined structures are thermally mismatched (e.g., a ball grid array which is reflow-soldered onto a PC-board). This stress is supposed to be known. By combination of Eqs. (3.2) and (3.3a) we therefore conclude that

$$\varepsilon = \frac{\sigma_0}{C_{11}^{\beta} - \frac{c^{\beta}-c}{c^{\beta}-c^{\alpha}}\left(C_{11}^{\beta} - C_{11}^{\alpha}\right)} + \left[\alpha_1^{\beta} - \frac{c^{\beta}-c}{c^{\beta}-c^{\alpha}}\left(\alpha_1^{\beta} - \alpha^{\alpha}\right)\right](T - T_{\mathrm{R}}) \tag{3.7}$$

is the explicit solution for the 1D strain, which is *not* constant in space, because of its dependence on the current concentration, c. Consequently, the strain needs to be constantly updated during the microstructural development, which manifests itself in the change of concentration.

3.2. The 1D-diffusion equation

When specialized to one dimension, $x_1 = x$, the diffusion equation reads:

$$\rho_0 \frac{\partial c}{\partial t} + \frac{\partial J}{\partial x} = 0. \tag{3.8}$$

The "extended" diffusion flux, J, becomes (cf., Eq. (1.2)):

$$J = -\rho_0 \left[M_1^{\beta} - \frac{c^{\beta}-c}{c^{\beta}-c^{\alpha}}\left(M_1^{\beta} - M^{\alpha}\right)\right] \frac{\partial}{\partial x}\left(\frac{\partial \psi}{\partial c} - \left[a_1^{\beta} - \frac{c^{\beta}-c}{c^{\beta}-c^{\alpha}}\left(a_1^{\beta} - a^{\alpha}\right)\right] \frac{\partial^2 c}{\partial x^2} + \frac{\partial e}{\partial c}\right). \tag{3.9}$$

For the derivative elastic strain energy density, e, with respect to the concentration, c, we may write according to Eqs. (1.2), (1.5), (1.11) and (3.2):

$$\begin{aligned} \frac{\partial e}{\partial c} &= \frac{1}{2}\frac{\partial}{\partial c}\left[\left(\varepsilon_{kl} - \varepsilon_{kl}^{*}\right) C_{klrs}\left(\varepsilon_{rs} - \varepsilon_{rs}^{*}\right)\right] \\ &= -\left[C_{11}^{\beta} - \frac{c^{\beta}-c}{c^{\beta}-c^{\alpha}}\left(C_{11}^{\beta} - C_{11}^{\alpha}\right)\right](\varepsilon - \varepsilon^{*})\frac{\alpha_1^{\beta} - \alpha^{\alpha}}{c^{\beta}-c^{\alpha}}\Delta T + \frac{1}{2}(\varepsilon - \varepsilon^{*})^2 \frac{C_{11}^{\beta} - C_{11}^{\alpha}}{c^{\beta}-c^{\alpha}}, \end{aligned} \tag{3.10}$$

and ε and ε^{*} are to be inserted from Eqs. (3.2) and (3.7).

3.3. Numerical procedures employed

By insertion of Eqs. (3.9) and (3.10), we arrive at:

$$\frac{\partial c}{\partial t} = \frac{M_1^\beta - M^\alpha}{c^\beta - c^\alpha}\frac{\partial c}{\partial x}\frac{\partial}{\partial x}\left(\frac{\partial \psi}{\partial c} - \left[a_1^\beta - \frac{c^\beta - c}{c^\beta - c^\alpha}\left(a_1^\beta - a^\alpha\right)\right]\frac{\partial^2 c}{\partial x^2} + \frac{\partial e}{\partial c}\right) + \left[M_1^\beta - \frac{c^\beta - c}{c^\beta - c^\alpha}\left(M_1^\beta - M^\alpha\right)\right]\frac{\partial^2}{\partial x^2}\left(\frac{\partial \psi}{\partial c} - \left[a_1^\beta - \frac{c^\beta - c}{c^\beta - c^\alpha}\left(a_1^\beta - a^\alpha\right)\right]\frac{\partial^2 c}{\partial x^2} + \frac{\partial e}{\partial c}\right). \tag{3.11}$$

The data presented in Eqs. (2.23a)–(2.26) seem to indicate that the mobility of the β-phase is dominant. Consequently, the last equation may be simplified as follows:

$$\frac{\partial c}{\partial t} = \frac{M_1^\beta}{c^\beta - c^\alpha}\frac{\partial c}{\partial x}\frac{\partial}{\partial x}\left(\frac{\partial \psi}{\partial c} - \left[a_1^\beta - \frac{c^\beta - c}{c^\beta - c^\alpha}\left(a_1^\beta - a^\alpha\right)\right]\frac{\partial^2 c}{\partial x^2} + \frac{\partial e}{\partial c}\right) + M_1^\beta \frac{c - c^\alpha}{c^\beta - c^\alpha}\frac{\partial^2}{\partial x^2}\left(\frac{\partial \psi}{\partial c} - \left[a_1^\beta - \frac{c^\beta - c}{c^\beta - c^\alpha}\left(a_1^\beta - a^\alpha\right)\right]\frac{\partial^2 c}{\partial x^2} + \frac{\partial e}{\partial c}\right). \tag{3.12}$$

However, as outlined in Section 2.2, there is still a certain level of insecurity in the mobility data, first, that no difference in the mobilities in the crystallographic axes of the tin-rich phase was reported and, second, that the mobility of the β-phase is dominant when compared to that of the α-phase. In order to assess the impact on coarsening of the latter, it seems appropriate to also numerically investigate the case of (nearly) *equal* mobilities in both phases. In this case, the relevant diffusion equation reads:

$$\frac{\partial c}{\partial t} = M_1^\beta \frac{\partial^2}{\partial x^2}\left(\frac{\partial \psi}{\partial c} - \left[a_1^\beta - \frac{c^\beta - c}{c^\beta - c^\alpha}\left(a_1^\beta - a^\alpha\right)\right]\frac{\partial^2 c}{\partial x^2} + \frac{\partial e}{\partial c}\right). \tag{3.13}$$

Eqs. (3.12) and (3.13) are solved by means of Discrete Fourier Transforms (DFT). Details of the fundamentals of this technique and its application to solid mechanics problems can be found in the papers of Suquet's group (Michel et al., 1999; Moulinec and Suquet, 1994, 1998), Khachaturyan's school (e.g., Wang et al., 1993a,b, 1994; Li and Chen, 1997), the Japanese group (e.g., Koyama and Miyazaki, 1994, 1998), Müller (1996, 1998) and Dreyer and Müller (2000). It should be noted that in the present work, the formalism as described in the latter two papers was used during the simulations. In particular, spatial derivatives in Fourier space [5] were approximated as follows:

$$Y\left[\frac{\partial \bullet}{\partial x}\right] = -\xi_x(s)Y[\bullet] + \mathrm{O}\left(h^2\right), \quad \xi_x(s) = -\frac{\mathrm{i}}{h}\sin\left(2\pi\frac{s}{N}\right), \quad s = 0, \ldots, N-1 \tag{3.14}$$

and

$$Y\left[\frac{\partial^2 \bullet}{\partial x^2}\right] = \xi_{xx}Y[\bullet] + \mathrm{O}\left(h^2\right), \quad \xi_{xx}(s) = \frac{2}{h^2}\left(\cos\left(2\pi\frac{s}{N}\right) - 1\right), \quad h = \frac{2\pi L}{N}, \tag{3.15}$$

where h denotes the grid spacing in real space, s identifies the position in discrete Fourier space, and N is the number of grid points.

If these two differentiation rules and a simple forward difference quotient in time are applied to Eqs. (3.12) and (3.13), we obtain:

[5] Quantities in (discrete) Fourier space are denoted by a hat or can be identified by a preceding Y.

$$\frac{\hat{c}^{n+1}-\hat{c}^{n}}{\frac{M_1^{\beta}}{c^{\beta}-c^{\alpha}}\Delta t} = Y\left(\frac{\partial c}{\partial x}\frac{\partial}{\partial x}\left(\frac{\partial \psi}{\partial c}-\left[a_1^{\beta}-\frac{c^{\beta}-c}{c^{\beta}-c^{\alpha}}\left(a_1^{\beta}-a^{\alpha}\right)\right]\frac{\partial^2 c}{\partial x^2}+\frac{\partial e}{\partial c}\right)\right)\Bigg|_{\hat{c}=\hat{c}^n}$$
$$+ Y\left(c\frac{\partial^2}{\partial x^2}\left(\frac{\partial \psi}{\partial c}-\left[a_1^{\beta}-\frac{c^{\beta}-c}{c^{\beta}-c^{\alpha}}\left(a_1^{\beta}-a^{\alpha}\right)\right]\frac{\partial^2 c}{\partial x^2}+\frac{\partial e}{\partial c}\right)\right)\Bigg|_{\hat{c}=\hat{c}^n} - c^{\alpha}\xi_{xx}\left(Y\left(\frac{\partial \psi}{\partial c}\right)\Bigg|_{\hat{c}=\hat{c}^n}\right.$$
$$\left. - \left[a_1^{\beta}-\frac{c^{\beta}}{c^{\beta}-c^{\alpha}}\left(a_1^{\beta}-a^{\alpha}\right)\right]\xi_{xx}\hat{c}^{n+1} - \frac{a_1^{\beta}-a^{\alpha}}{c^{\beta}-c^{\alpha}}Y\left(c\frac{\partial^2 c}{\partial x^2}\right)\Bigg|_{\hat{c}=\hat{c}^n} + Y\left(\frac{\partial e}{\partial c}\right)\Bigg|_{\hat{c}=\hat{c}^n}\right) \tag{3.16}$$

and

$$\frac{\hat{c}^{n+1}-\hat{c}^{n}}{M_1^{\beta}\Delta t} = \xi_{xx}\left(Y\left(\frac{\partial \psi}{\partial c}\right)\Bigg|_{\hat{c}=\hat{c}^n} - \left[a_1^{\beta}-\frac{c^{\beta}-c}{c^{\beta}-c^{\alpha}}\left(a_1^{\beta}-a^{\alpha}\right)\right]\xi_{xx}\hat{c}^{n+1} - \frac{a_1^{\beta}-a^{\alpha}}{c^{\beta}-c^{\alpha}}Y\left(c\frac{\partial^2 c}{\partial x^2}\right)\Bigg|_{\hat{c}=\hat{c}^n}\right.$$
$$\left. + Y\left(\frac{\partial e}{\partial c}\right)\Bigg|_{\hat{c}=\hat{c}^n}\right). \tag{3.17}$$

This way, a partially implicit scheme can be obtained that, based on our experience, seems to allow the use of larger time steps and also guarantees stability and convergence (for a similar strategy see also Küpper and Masbaum, 1994).

4. Results and discussion

4.1. General remarks

All simulations were performed using a dimensionless time, which, in the case of dominant β-mobility, was given by

$$\tilde{t} = \frac{M_1^{\beta}}{c^{\beta}-c^{\alpha}}\frac{10^9\ \mathrm{J\,m^{-3}}}{L^2}t = \begin{cases} \frac{t}{4.97\ \mathrm{s}} & \text{at } 125^{\circ}\mathrm{C}, \\ \frac{t}{2.23\times 10^4\ \mathrm{s}} & \text{at } 20^{\circ}\mathrm{C}, \end{cases} \tag{4.1}$$

and, in the case of equal mobilities of both phases, by

$$\tilde{t} = M_1^{\beta}\frac{10^9\ \mathrm{J\,m^{-3}}}{L^2}t = \begin{cases} \frac{t}{5.60\ \mathrm{s}} & \text{at } 125^{\circ}\mathrm{C}, \\ \frac{t}{2.29\times 10^4\ \mathrm{s}} & \text{at } 20^{\circ}\mathrm{C} \end{cases} \tag{4.2}$$

in Eqs. (3.16) and (3.17), respectively. The time-step chosen was

$$\Delta\tilde{t} = 10^{-5}. \tag{4.3}$$

In the following subsections, the temporal development of the concentration profile, $c = \tilde{c}(x,t)$, will be presented. For all simulations, the discretization in space was $N = 128$. Also, to allow for a direct comparison, the initial concentration profile was the same for all simulations and given by an essentially constant eutectic concentration level with one slight fluctuation as indicated in Fig. 8.

As indicated in Section 2, the development of concentration, in other words the coarsening process, will be studied for two different temperatures, i.e., $T_{\mathrm{high}} = 125^{\circ}\mathrm{C}$ and $T_{\mathrm{low}} = 20^{\circ}\mathrm{C}$. In view of the equilibrium phase diagram of the SnPb system shown in Fig. 9, it is tempting to interpret this type of study as a quenching process from the temperature of the eutectic point, $T_{\mathrm{eut}} = 183^{\circ}\mathrm{C}$, [6] and the corresponding

[6] Note that this temperature level was also chosen to be the stress-free temperature, T_{R}, required in Eq. (3.7).

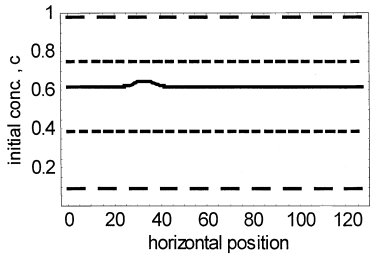

Fig. 8. Initial concentration profile at the eutectic level showing one slight fluctuation; in addition, the equilibrium (Maxwell) concentration levels (– – –) as well as the spinodal concentrations (- - -) at 125°C are shown.

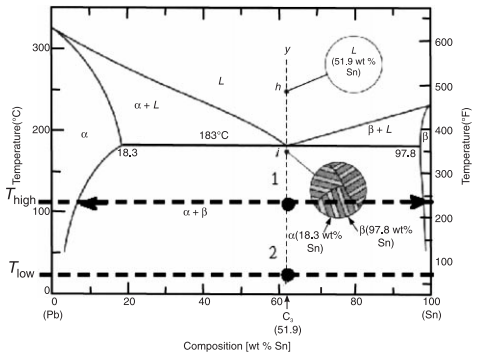

Fig. 9. The phase diagram of the binary alloy SnPb according to Callister (1997), see text for an explanation of the additional markings.

concentration down to lower temperature levels, points 1 and 2, to be followed by instantaneous separation of both phases to assume the equilibrium concentration levels, as indicated by the arrows.

Clearly, points 1 and 2 are highly unstable and will never be able to be reached in practice. However, it should be noted that the model accounts for this instability in the sense that the slightest fluctuation from the eutectic concentration will lead to instantaneous phase separation. Moreover, it should be pointed out that no attempt is made in this study to solve the heat conduction problem associated with the cooling process and the change in temperature.

Besides the development of concentration profiles, the diffusion flux, i.e., the driving force will also be shown. Depending on whether the case of dominant β-phase mobility or equal mobilities of both phases is considered, different quantities will be depicted (cp., Eq. (3.9)) namely, for a dominant β-mobility:

$$\frac{JL}{-\rho_0 M_1^{\beta} 10^9\ \mathrm{J\,m^{-3}}} = \frac{c^{\beta}-c}{c^{\beta}-c^{\alpha}}\frac{\partial}{\partial\tilde{x}}\left(\frac{\partial\psi}{\partial c} - \left[a_1^{\beta} - \frac{c^{\beta}-c}{c^{\beta}-c^{\alpha}}\left(a_1^{\beta}-a^{\alpha}\right)\right]\frac{\partial^2 c}{\partial x^2} + \frac{\partial e}{\partial c}\right) \tag{4.4}$$

and for equal mobilities:

$$\frac{JL}{-\rho_0 M_1^{\beta} 10^9\ \mathrm{J\,m^{-3}}} = \frac{\partial}{\partial\tilde{x}}\left(\frac{\partial\psi}{\partial c} - \left[a_1^{\beta} - \frac{c^{\beta}-c}{c^{\beta}-c^{\alpha}}\left(a_1^{\beta}-a^{\alpha}\right)\right]\frac{\partial^2 c}{\partial x^2} + \frac{\partial e}{\partial c}\right), \tag{4.5}$$

where

$$\tilde{x} = \frac{x}{L}. \tag{4.6}$$

4.2. Development of concentration at low and high temperatures

This subsection focuses on the development at low and high temperatures due to the influence of the free energy and surface energies only. In other words, the mechanical energy term shown in Eqs. (3.11) and (3.12) or Eqs. (4.4) and (4.5) will be omitted here.

Figs. 10, 11 and 12, 13 show the concentrations and fluxes at $T_{\text{high}} = 125°\text{C}$ and $T_{\text{low}} = 20°\text{C}$, respectively. [7] Judging from these results, we may say that the peak width at high a temperature seems more evenly spread than at low temperatures. A few peaks at a high temperature do not seem to have completely reached the equilibrium concentration, c^{α}, as yet. However, increasing the amount of time steps would not lead to a further change in the concentration profile, at least not immediately. This is certainly due to the relatively small driving force as evident by the flux shown in the last picture of the sequence shown in Fig. 11.

Clearly, the time factors involved in approaching equilibrium are extremely different for the two temperatures considered. If we use the data provided in Eq. (4.1), we must conclude that the last pictures of Figs. 10 and 12 correspond to roughly 25 s and 31 h, respectively. This is in qualitative agreement with the experimental observations of Harris et al. (1991) as discussed in Section 1.2 of this paper. If we assume the structures shown in the last micrographs of the first two rows of Fig. 4 to be very close to equilibrium, then the temporal difference to reach this state can be characterized by a fraction of 300 h/64 d $\approx 1:5$. In contrast to this, the theoretically obtained figures yield 25 s/31 h $\approx 1:4460$. This quantitative discrepancy is due to two reasons, first, to the insecurity of the mobility coefficient and its dependence on temperature and, second, to the fact that equilibrium has not quite been reached in the case of the high temperature profiles. Further studies of the further temporal development are obviously required, which necessitate optimization of the numerical techniques used. In this context, it must also be pointed out that in order to directly compare the coarseness at different temperatures, it is necessary to look at concentration profiles predicted for the same absolute time. For example, the coarseness of the last picture shown in Fig. 10 should be compared to a situation before the first picture shown in Fig. 12.

If we finally compare the concentration profiles predicted by the model that uses equal mobility coefficients for both phases (Fig. 14) to the corresponding situation for dominant mobility (Fig. 12), we must conclude that the predicted (equilibrium) microstructure of the latter seems to be of a slightly more heterogeneous nature. And indeed, in comparison with experimental evidence (the first picture in the sequence shown in Fig. 4), a certain distribution of peaks widths seems to be realistic. This observation indirectly supports the correctness of the strongly different mobility data for both phases as provided by Ghosh and Liu (1998).

4.3. The influence of thermo-mechanical stresses and strains

Fig. 15 presents the concentrations, if a tensile stress of magnitude $\sigma_0 = 1000$ MPa is included during the evaluation of Eq. (3.12) in combination with Eqs. (3.7) and (3.10). In comparison with the corresponding pictures from Fig. 10, we conclude that the tensile stress temporarily leads to a slight acceleration and intensification of the coarsening process. However, it does not seem to influence the longer term development of the microstructure dramatically. It should be noted that this stress is already extremely high. Nevertheless, there is experimental evidence that there is some amount of stress/strain localization and amplification in the vicinity of SnPb grain boundaries (Bonda and Noyan, 1996) that makes this choice a little less artificial.

In order to see a dramatic impact of stress on the microstructural development, it becomes necessary to consider somewhat unrealistic stress levels as indicated in the sequence shown in Fig. 16, where

[7] The numbers shown next to the abscissa label refer to the corresponding dimensionless times. The length scale shown is $2\pi L = 10^{-6}$ m, $N = 128$.

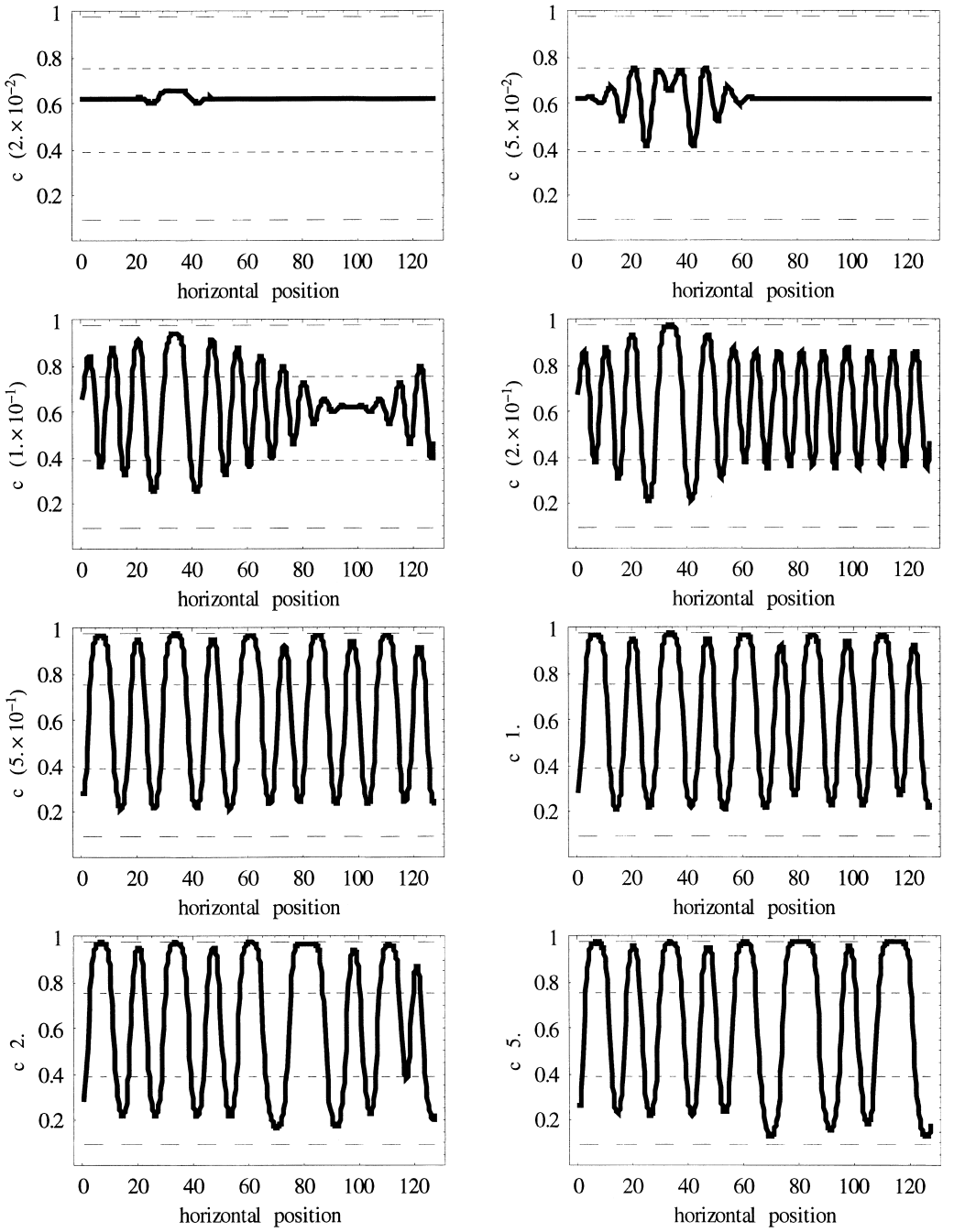

Fig. 10. Development of concentration, dominant mobility of the β-phase, no thermo-mechanical loads, $T_{high} = 125°C$.

$\sigma_0 = 10000$ MPa has been set. Obviously, the predicted microstructure is then clearly much coarser than the one shown in the corresponding picture of Fig. 10.

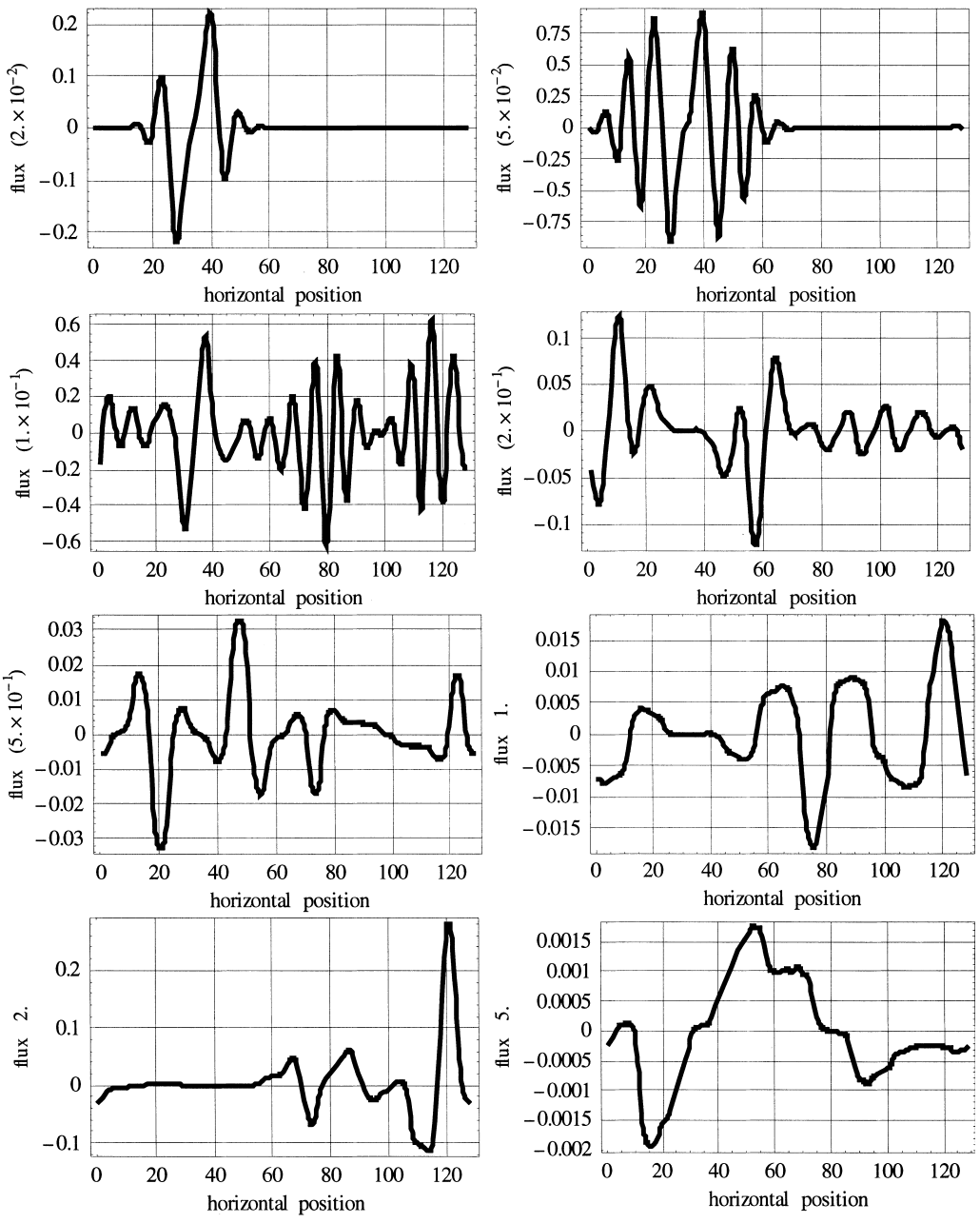

Fig. 11. Development of diffusion flux, dominant mobility of the β-phase, no thermo-mechanical loads, $T_{\text{high}} = 125°\text{C}$.

5. Conclusions and outlook

A theoretical framework has been presented that, after numerical evaluation, allows us to quantitatively predict the coarsening process observed during aging of (eutectic) SnPb solders. The agreement between the theoretically predicted and experimentally observed temporal development of an (unstressed) microstruc-

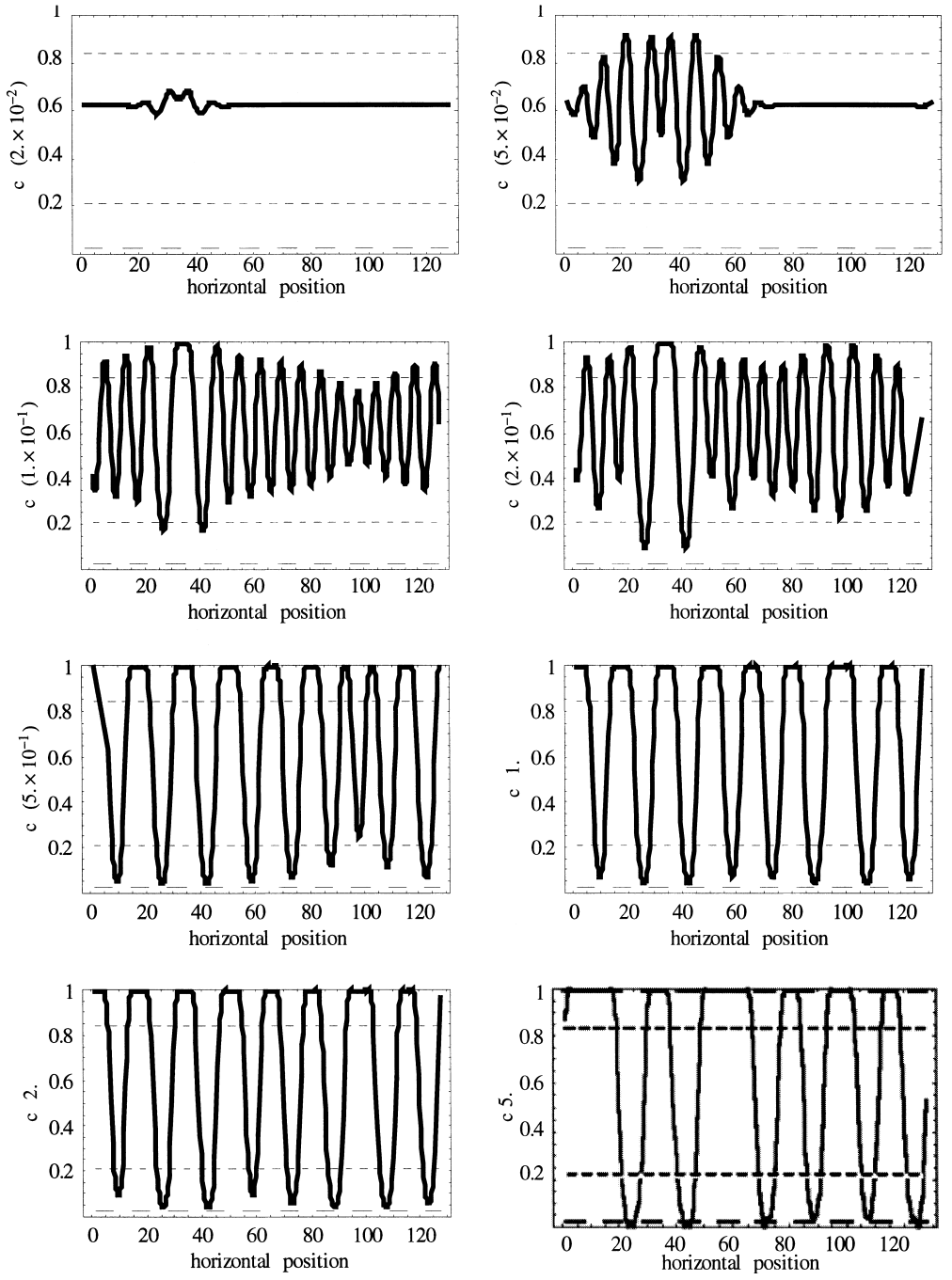

Fig. 12. Development of concentration, dominant mobility of the β-phase, no thermo-mechanical loads, $T_{low} = 20°C$.

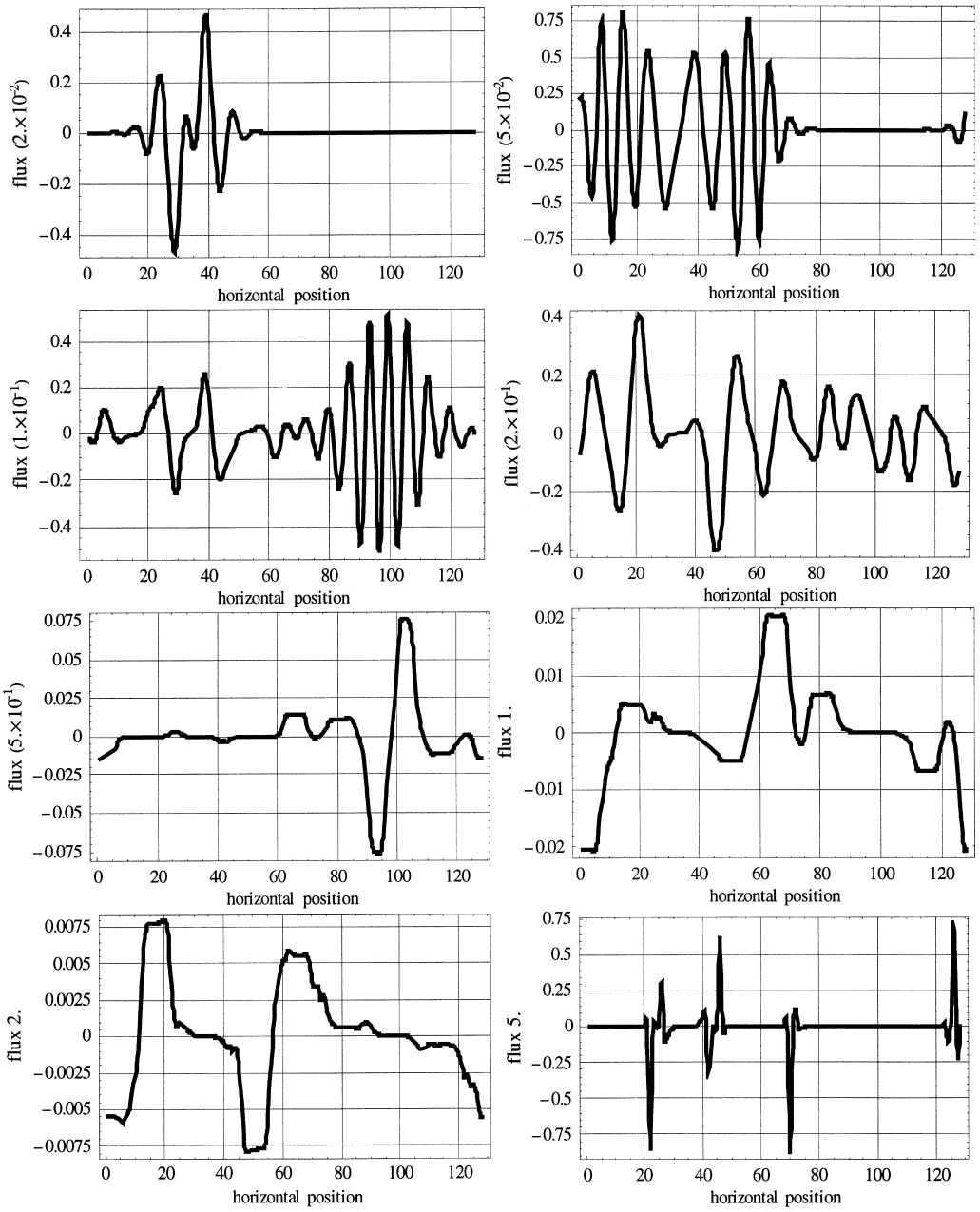

Fig. 13. Development of diffusion flux, dominant mobility of the β-phase, no thermo-mechanical loads, $T_{low} = 20°C$.

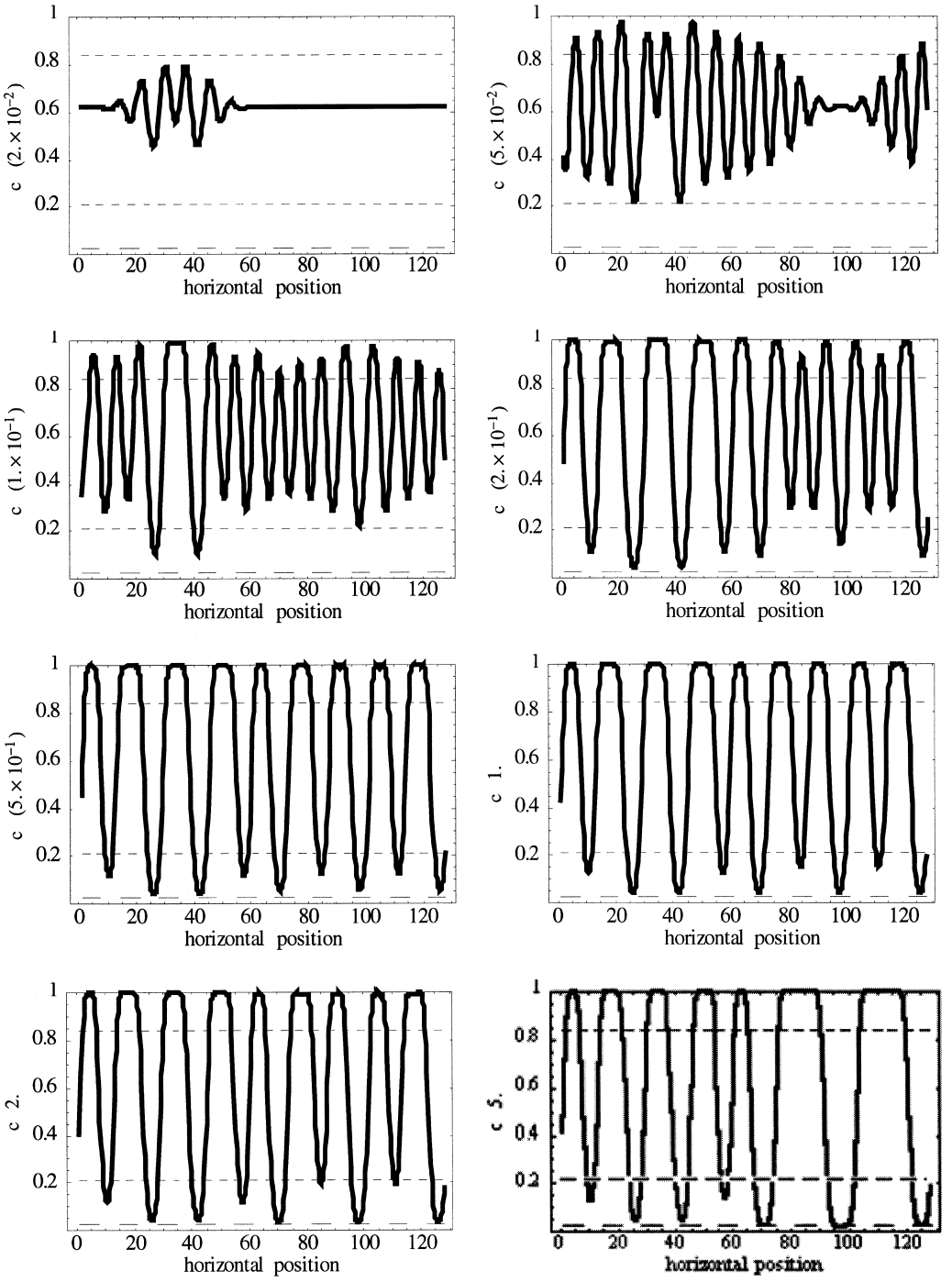

Fig. 14. Development of concentration, equal mobilities of both phases, no thermo-mechanical loads, $T_{low} = 20°C$.

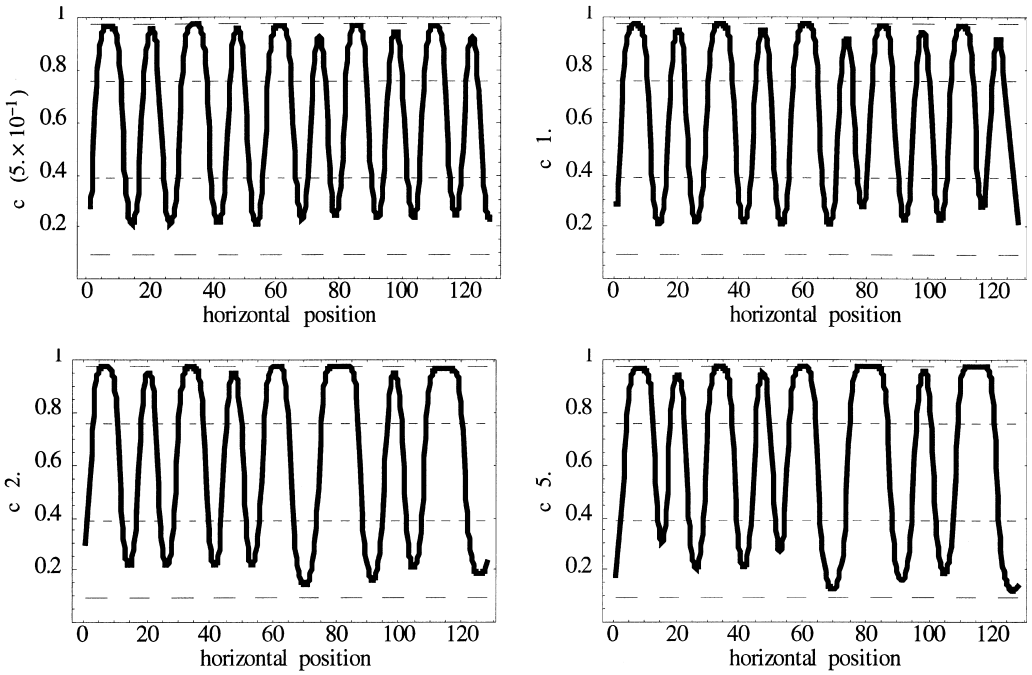

Fig. 15. Development of concentration, dominant mobility of the β-phase, with thermo-mechanical loads, $\sigma = 1000$ MPa, $T_{\text{high}} = 125°\text{C}$.

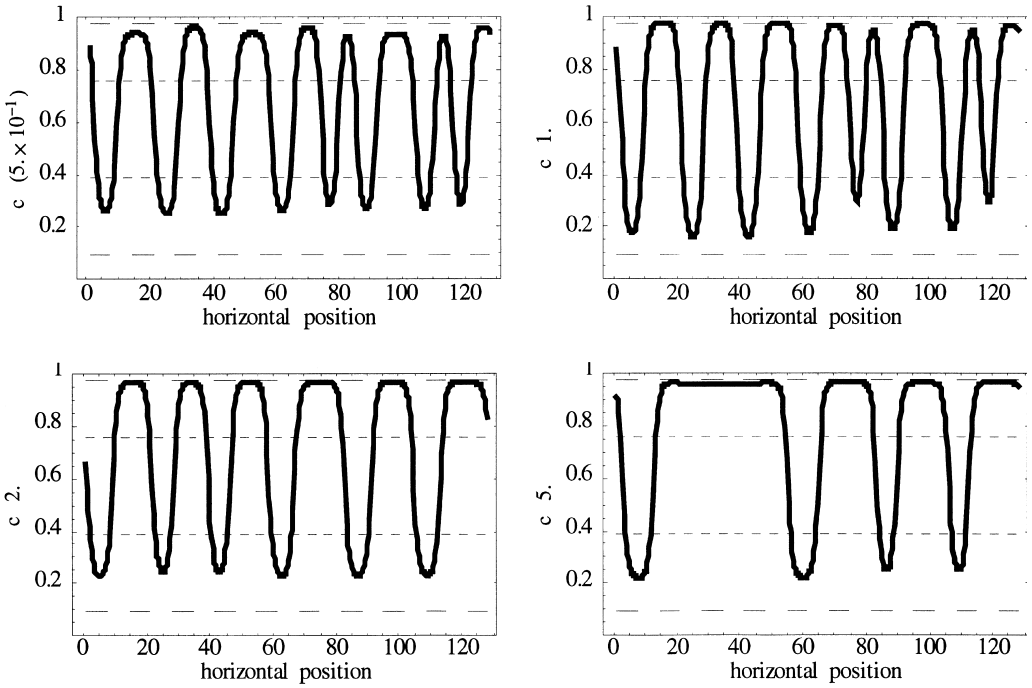

Fig. 16. Development of concentration, dominant mobility of the β-phase, with thermo-mechanical loads, $\sigma = 10000$ MPa, $T_{\text{high}} = 125°\text{C}$.

ture at low and high temperatures is reasonably good. It could be improved by adjusting critical material parameters, such as the free energy of the system and the mobility coefficients, which are necessary to describe diffusion in both phases. However, this has *not* been attempted in this work as the parameters that are used in a decent and honest theory should stem from independently performed measurements.

As far as the influence of thermo-mechanical loads on the coarsening is concerned, it is fair to say that within the scope of the presented theory, extremely high stress levels are necessary to clearly demonstrate an effect. However, it is also fair to say that experimental evidence regarding the influence of stress on phase separation in SnPb solders has not sufficiently been quantified so far. Both experiments as well as theory need to be critically analyzed, suitably modified and extended. As far as the theory is concerned, it might become necessary to make use of higher gradient terms as described in the appendix of the work by Dreyer and Müller (2000). The difficulty with such terms is to quantify the corresponding material parameters. However, from an atomistic point of view, it seems possible to relate these parameters to the potentials between the atomic species and derivatives thereof. These, in turn, can be obtained from the free energies of the system in question, which follow from macroscopic experiments.

Further studies are currently underway, which will help to clarify the following issues:

- extension of the presented work to two and three dimensions, [8]
- improvement of the numerical algorithms (DFT) used to easily enable long-term development studies,
- discussion of stability and convergence of the algorithms,
- influence of the initial condition on the predicted temporal development,
- a quantitative comparison of the size of the predicted and experimentally observed size of the microstructures within an RVE, [9]
- application of the theory to other binary solder systems,
- extension and application of the theory to non-binary alloys.

Acknowledgements

The foundations to this paper were laid during a visit of W.H.M. to the Weierstraß Institute in the spring of 1999. The stay was financially supported by the Gottfried Wilhelm Leibnitz Fund. Moreover, the authors wish to thank Ms. Yvonne van Leeuwen, Laboratory of Materials Science, Technische Universiteit Delft, for valuable help with the materials data.

References

Albrecht, H.-J., Gamalski, J., 1996. Fatigue properties of BGA solder joints: a comparison of thermal and power cycle tests. Proc. SMI '96, San Jose, pp. 61–80.

Bonda, N.R., Noyan, I.C., 1996. Effect of the specimen size in predicting the mechanical properties of PbSn solder alloys. IEEE Trans. Comp., Packag., Manufact. Technol. – Part A 19 (2), 208–212.

Brandes, E.A. (Ed.), 1983. Smithells Metals Reference Book, sixth ed. Butterworths, London.

[8] A multidimensional numerical analysis will certainly have an impact on the influence of the thermo-mechanical term presented in this paper on microstructural development. However, the qualitative analysis presented in the work by Dreyer and Müller (1999) indicates that the stresses required even in that case will still be very large.

[9] Cline (1984), Fredriksson (1987), and Lee (1990) report on the eutectic spacing of lamella in SnPb materials. Their results are based on 2D evaluations. It is for that reason that no attempt was made to establish a correlation between theory and experiments. However, it can be said that on first glance, the size of the microstructures predicted from 1D modeling (>0.2 μm, <1 μm) is in agreement with the experiments for the temperature range considered.

Callister Jr., W.D., 1997. Materials Science and Engineering – An Introduction. Wiley, New York.
Cahn, J.W., Hilliard, J.E., 1958. Free energy of a non-uniform system. I. Interfacial free energy. J. Chem. Phys. 28 (1), 258–267.
Chada, S., Herrmann, A., Laub, W., Fournell, R., Shanguan, D., Achari, A., 1997. Microstructural investigation of Sn–Ag and Sn–Pb–Ag solder joints. Soldering and Surface Mount Technol. 26, 9–21.
Cline, H.E., 1984. Interlamellar spacing in directionally solidified eutectic thin films. Metall. Trans. A 15A, 1013–1017.
Decker, D.L., Weiss, J.D., Vanfleet, H.B., 1977. Diffusion of Sn in Pb to 30 kbar. Phys. Rev. B 16 (6), 2392–2394.
Dreyer, W., Müller, W.H., 2000. A study of the coarsening in tin/lead solders. Int. J. Solids Struct. 37 (28), 3841–3871.
Fredriksson, H., 1987. On the mechanism of eutectic solidification. Mater. Lett. 5 (11,12), 457–459.
Ghosh, G., Liu, Z.-K., 1998. Modeling the atomic transport kinetics in high-lead solders. J. Electron. Mater. 27 (12), 1362–1366.
Harris, P.G., Chaggar, K.S., Whitmore, M.A., 1991. The effect of ageing on the microstructure of 60:40 tin–lead solders. Soldering and Surface Mount Technol. 7, 20–23.
Hauck, T., Linnenbrock, K., Neumann, S., Ferber, F., Herrmann, K.P., 2000. Flip-Chip Technologie in der Mikroelektronik Mechanische Zuverlässigkeit, Wärmespannungsbruch. Proc. of the 32. Veranstaltung des DVM-Arbeitskreises Bruchvorgänge Festigkeits- und Bruchverhalten von Fügeverbindungen, Berlin, February 2000, 53–62.
Koyama, T., Miyazaki, T., 1994. Computer simulation of phase decomposition in real alloy systems. In: Johnson, W.C., Howe, J.M., Laughlin, D.E., Soffa, W.A. (Eds.), Solid→Solid Phase Transformations. The Minerals, Metals and Materials Society, pp. 365–370.
Koyama, T., Miyazaki, T., 1998. Computer simulation of phase decomposition in two dimensions based on a discrete type non-linear diffusion equation. Mater. Trans. JIM. 39 (1), 169–178.
Küpper, T., Masbaum, N., 1994. Simulation of particle growth and Ostwald ripening via the Cahn–Hilliard equation. Acta Metall. Mater. 42 (6), 1847–1858.
Lau, J.H. (Ed.), 1995. Ball Grid Array Technology, SMTnet.
Lau, J.H., Chang, C., 1999. TMA, DMA, DSC and TGA of lead free solders. Soldering and Surface Mount Technol. 11/2, 17–24.
Lee, J.-K., 1990. Diskontinuierliche Auflösung und Ausscheidung in Pb–Sn-Mischkristallen. Ph.D. Thesis, MPI Stuttgart.
Lee, N.-C., 1997. Getting ready for lead-free solders. Soldering and Surface Mount Technol. 26, 65–69.
Li, D.Y., Chen, L.Q., 1997. Computer simulation of morphological evolution and rafting of particles in Ni-based superalloys under applied stress. Scripta Materialia 37 (9), 1271–1277.
Lord, P.C., Witt, M.C., Bilham, R., Edwards, T., King, C., 1997. Rating lead-free BGA solder alloys. SMT, pp. 86–89.
Low, M.K., Williams, D.J., 1998. European environmental legislation in electronics and its potential impact on far eastern suppliers. Proc. EPTC '98, Singapore, 1998, IEEE, Piscataway, NJ, pp. 206–213.
Michel, J.C., Moulinec, H., Suquet S, 1999. Effective properties of composite materials with periodic microstucture: a computational approach. Comput. Meth. Appl. Mech. Engng. 172 (1–4), 109–143.
Moulinec, H., Suquet, P., 1994. A fast numerical method for computing the linear and nonlinear mechanical properties of composites. C.R. Acad. Sci. Paris 318 (II), 1417–1423.
Moulinec, H., Suquet, P., 1998. A numerical method for computing the overall response of nonlinear composites with complex microstructure. Comp. Meth. Appl. Mech. Engng. 157 (1–2), 69–94.
MTData, 1998. NPL Databank for Materials Thermochemistry. National Physical Laboratory, Teddington, Middlesex.
Müller, W.H., 1998. Fourier transforms and their application to the formation of textures and changes of morphology in solids. Proc. IUTAM Symposium on Transformation Problems in Composite and Active Materials, Cairo, 1997, Kluwer Academic Publishers, Dordrecht, pp. 61–72.
Nylén, M., Hutchinson, B., Gustavsson, U., 1997. Microstructural degradation of solder. In: Proc. Micro Materials, Micro Mat '97, Berlin, pp. 890–895.
Oberschmidt, J., Kim, K.K., Gupta, D., 1982. Grain-boundary diffusion in some Pb–Sn alloys. J. Appl. Phys. 53 (8), 5672–5677.
Ozmat, B., 1990. A nonlinear thermal stress analysis of surface mount solder joints. Proc. 40th IEEE ECTC, vol. II, 959–972.
Pao, Y.-H., 1992. A fracture mechanics approach to thermal fatigue life prediction of solder joints. IEEE Trans. Comp., Hybrids, Manufact. Technol. 15 (4), 559–570.
Sen, S.K., Ghorai, A., 1989. The diffusion of tin in lead. Philosoph. Magaz. A 39 (3), 707–712.
Wang, Y., Chen, L.-Q., Khachaturyan, A.G., 1993a. Kinetics of strain-induced morphological transformation in cubic alloys with a miscibility gap. Acta Metall. Mater. 41 (1), 279–296.
Wang, Y., Wang, H., Chen, L.-Q., Khachaturyan, A.G., 1993b. Shape evolution of a coherent tetragonal precipitate in partially stabilized cubic ZrO_2: a computer simulation. J. Am. Ceram. Soc. 76 (12), 3029–3033.
Wang, Y., Wang, H., Chen, L.-Q., Khachaturyan, A.G., 1994. Computer simulation of microstructure evolution in coherent solids. In: Johnson, W.C., Howe, J.M., Laughlin, D.E., Soffa, W.A. (Ed.), Solid→Solid Phase Transformations, The Minerals, Metals and Materials Society, pp. 245–265.